Journal of Volcanology and Geothermal Research 420 (2021) 107406

Contents lists available at ScienceDirect

Journal of Volcanology and Geothermal Research

journal homepage: www.elsevier.com/locate/jvolgeores

A century of ongoing silicic volcanism at Cordón Caulle, Chile: New constraints on the magmatic system involved in the 1921–1922, 1960 and 2011–2012 eruptions

Gilles Seropian [a,*], C. Ian Schipper [b], Lydia J. Harmon [c], Sarah L. Smithies [a], Ben M. Kennedy [a], Jonathan M. Castro [d], Brent V. Alloway [e,f], Pablo Forte [d,g]

[a] School of Earth and Environment, University of Canterbury, Christchurch, New Zealand
[b] School of Geography, Environmental and Earth Sciences, Victoria University of Wellington, Wellington, New Zealand
[c] Earth and Environmental Sciences, Vanderbilt University, Nashville, USA
[d] Institute of Geosciences, Johannes Gutenberg-Universität Mainz, Mainz, Germany
[e] School of Environment, The University of Auckland, Auckland, New Zealand
[f] Instituto de Geografía, Pontificia Universidad Católica de Chile, Santiago, Chile
[g] Instituto de Estudios Andinos, UBA-CONICET, Buenos Aires, Argentina

ARTICLE INFO

Article history:
Received 23 June 2021
Received in revised form 17 September 2021
Accepted 21 September 2021
Available online 25 September 2021

Keywords:
Cordón Caulle
Geobarometry
Rhyolite-MELTS
Silicic volcano
Geochemistry
Seismically-triggered

ABSTRACT

Cordón Caulle in southern Chile has produced three dacitic to rhyolitic fissure eruptions over the past century (in 1921–1922, 1960 and 2011–2012), and thereby provides an ideal opportunity to examine the architecture of its underlying silicic system. While the 2011–2012 eruption has been extensively studied, comparatively little is known about the 1921–1922 and 1960 events. Major-element matrix glass analyses from the 1960 products (71.5 wt.% SiO_2) are indistinguishable from the 2011–2012 data (72.2 wt.% SiO_2), but the 1921–1922 analyses form a discrete, slightly less evolved sub-population (69.0 wt.% SiO_2). We utilise rhyolite-MELTS geobarometry to estimate both the storage and extraction depths of all three magmas. For all three eruptions, magma was stored in the shallow crust, between 80–150 MPa (3.5–6.6 km). The 2011–2012 magma body spanned this whole depth range but the 1921–1922 and 1960 magma bodies were more confined in pressure, at 90–112 MPa (4.0–5.0 km) and 123–143 MPa (5.4–6.3 km) respectively. Melt extraction from a parental crystal-mush occurred in the range 70–200 MPa (3.1–9.0 km) for all three eruptions, suggesting contiguous melt segregation and storage in the shallow crust. Finally, we discuss whether the deeper magma storage in 1960 reflects the influence of a seismic trigger by events associated with the M_w9.5 Great Chilean earthquake.

1. Introduction

Understanding magma generation, storage and eruption trigger mechanisms at silicic volcanoes constitutes one of the great challenges of modern volcanology (Acocella, 2014). Significant advances have occurred since the early "big vat" models (Bowen, 1915) that envisioned large pools of continuous and convecting crystal-poor melt residing in the crust. We are now armed with models of silicic melt originating from highly crystalline mushes extending throughout the crust (e.g. Bachmann and Huber, 2016; Cashman et al., 2017). Nevertheless, very few rhyolitic eruptions have been directly observed, with only three such terrestrial eruptions occurring over the past 50 years, at Da'Ure, Ethiopia in 2005 (Ayele et al., 2007), Chaitén, Chile in 2008–2010 (Lara, 2009) and Cordón Caulle, Chile in 2011–2012 (Castro et al., 2013). Studying a system that has been observed erupting provides a unique opportunity to relate the geological record to the eruption dynamics (e.g. Castro and Dingwell, 2009; Saunders et al., 2012; Schipper et al., 2013; Pistolesi et al., 2015).

The 2011–2012 Cordón Caulle event was the largest of these three recent historic eruptions (and to date, is the largest of the twenty-first century). Despite its remote Andean location, it was well studied, with satellite remote sensing data playing a significant role (e.g. Jay et al., 2014; Castro et al., 2016; Coppola et al., 2017). Several field investigations were able to make direct observations of eruptive phenomena, as well as collect proximal ejecta samples for analysis (e.g. Schipper et al., 2013; Tuffen et al., 2013; Pistolesi et al., 2015; Paisley et al., 2019). Ash collection (in time-series) was also undertaken in medial to distal locations throughout the eruption (e.g. Daga et al., 2014; Bertrand et al., 2014; Alloway et al., 2015; Bonadonna et al., 2015a).

* Corresponding author.
E-mail address: gilles.seropian@pg.canterbury.ac.nz (G. Seropian).

https://doi.org/10.1016/j.jvolgeores.2021.107406

In addition to the 2011–2012 eruption, two silicic eruptions occurred at Cordón Caulle in 1921–1922 and 1960 (Lara et al., 2004). The occurrence of closely spaced explosive activity centred at Cordón Caulle provides a unique opportunity to explore temporal and spatial changes associated with this potentially long-lived and frequently erupting silicic system.

Constraining the pre-eruptive architecture of the magmatic reservoir and plumbing system that fuelled the 2011–2012 eruption has been a key objective of the past decade, with a range of field, remote sensing, experimental and numerical techniques (Castro et al., 2013, 2016; Schipper et al., 2013, 2021; Jay et al., 2014; Wendt et al., 2017; Delgado et al., 2018). However, the 1921–1922 and 1960 events have received much less attention. Based on the geochemical similarity of the three events, it is generally assumed that they were derived from the same magma reservoir (Jay et al., 2014), but a direct test of this assumption is still lacking.

The structure and eruptive history of Cordón Caulle are also intimately linked to the regional tectonics (Lara et al., 2004, 2006a; Wendt et al., 2017). Both the 1960 and 2011–2012 eruptions occurred after large tectonic earthquakes. The 1960 M_w9.5 Great Chilean earthquake is generally considered to have directly triggered the volcanic eruption (e.g. Barrientos, 1994; Manga and Brodsky, 2006; Walter and Amelung, 2007). Similarly, a possible association has been considered between the 2010 M_w8.8 Maule earthquake and the 2011–2012 eruption, though the link remains tenuous (Bonali et al., 2013; Jay et al., 2014). Thus, Cordón Caulle constitutes an ideal field laboratory to examine earthquake-volcano interactions.

In this contribution, we report major element composition of the matrix glass from the 1921–1922, 1960 and 2011–2012 products. We then constrain both the storage and extraction depths for all three eruptions using rhyolite-MELTS geobarometry (Gualda and Ghiorso, 2014; Harmon et al., 2018). Finally, we explore whether a deeper storage depth in 1960 could be an indicator of a tectonic trigger for this event.

2. Geological setting

Cordón Caulle (40.5°S, 72.2°W) is a 15 × 4Ckm fissure system, aligned NW-SE, within the larger Puyehue-Cordón Caulle Volcanic Complex (PCCVC) in the Southern Volcanic Zone of the Chilean Andes (Fig. 1). The PCCVC intersects the NNE-trending Liquiñe-Ofqui fault zone, a major intra-arc fault system of the southern Andes (Cembrano et al., 1996; Cembrano and Lara, 2009). The last three significant (VEI ≥3) PCCVC eruptions occurred at Cordón Caulle, in 1921–1922, 1960 and 2011–2012 (Gerlach et al., 1988; Lara et al., 2006b; Singer et al., 2008; Castro et al., 2013). All three eruptions produced lava flows which erupted from separate vents (Fig. 1).

The 1921–1922 and 1960 eruptions are poorly documented, mostly due to the volcano's remoteness and the lack of monitoring institutions at that time. The two eruptions were similar in style, intensity and bulk geochemistry (Lara et al., 2006b). Both eruptions started with an initial sub-Plinian phase (with an estimated 6 and 9 km plume height respectively, Hantke (1940), Katsui and Katz (1967)), followed by hybrid venting of ash and lava extrusion (in the case of the 1960 event; Lara et al., 2004) and then emplacement of lava. Bulk lava composition is consistently rhyodacitic (68.5–70 wt.% SiO_2, Gerlach et al. (1988)), with an estimated ~0.4 km^3 dense rock equivalent (DRE) erupted material produced in the 1921–1922 eruption, and an estimated ~0.25 km^3 in 1960 (Lara et al., 2006b). Both eruptions were fissure eruptions, forming two distinct parallel series of aligned vents (Fig. 1). The 1960 eruption is notable as it started only 38 h after the M_w9.5 Great Chilean earthquake, the largest earthquake ever recorded with instrumental seismological observations (Lara et al., 2004). It is thus often considered a prime example of a seismically-triggered eruption (e.g. Barrientos, 1994; Manga and Brodsky, 2006; Walter and Amelung, 2007). The 1921–1922 eruption is not known to be associated with any major regional tectonic event.

The 2011–2012 eruption was extensively monitored and studied (e.g. Castro et al., 2013; Jay et al., 2014; Pistolesi et al., 2015). The eruptive sequence is broadly similar to 1921–1922 and 1960 – initial Plinian phase, followed by hybrid explosive-effusive activity and prolonged effusion of lava. The magnitude of the eruption was however much larger (plume height of 14 km, ~2.7 km^3 DRE total erupted volume; Castro et al., 2013; Pistolesi et al., 2015; Bonadonna et al., 2015b; Delgado et al., 2019). Bulk rock compositions are nearly identical to those of the 1921–1922 and 1960 products (69.5 wt.% SiO_2, Castro et al., 2013). Though it may have begun as a fissure eruption, the 2011–2012 eruptive activity quickly focused to a single vent (Schipper et al., 2013).

3. Methods

3.1. Sample collection

We conducted two fieldwork campaigns at Cordón Caulle in 2016 and 2017. We first collected pumice lapilli from the distal fall deposits of the 1921–1922, 1960 and 2011–2012 eruptions at a section located close to Cardenal-Samoré Pass, on the border between Chile and Argentina, 20–30 km ESE of the different vents (location PCC-DIST in Fig. 1). We then collected pumice lapilli from proximal deposits at two locations near the lava flows (1921–1922 samples at PCC-PROX1 and both 1960 and 2011–2012 samples at PCC-PROX2, Fig. 1). A total of 17 pumice lapilli samples (nine from 1921–1922, six from 1960 and two from 2011–2012) were prepared in polished thin sections for geochemical analysis. Representative backscattered electron (BSE) images of our thin sections are shown in Fig. 2. These were acquired on a JEOL IT-300 scanning electron microscope at the University of Canterbury, with a 15 kV accelerating voltage, a 40 nA beam current and a 15 mm working distance.

3.2. Geochemical analysis

Major element compositions and volatile (S, F, Cl) contents of matrix glasses were determined by electron probe microanalysis (EPMA) with a JEOL JXA-8230 Superprobe at Victoria University of Wellington (VUW). We followed the same procedure as that of Schipper et al. (2019), which is summarized below.

For major elements, we used a 15 kV accelerating voltage, 8.0 nA current, peak/background count times of 30 s/15 s, and a beam defocused to 10 μm. Sodium was measured first, with shorter times (10 s/5 s) and at a fixed peak position, to avoid a peak search procedure and minimize volatilisation. Analyses were calibrated against a suite of standards (Jarosewich et al., 1980): VG-A99 basaltic glass standard for Ca, Mg and Fe; VG-568 rhyolitic glass standard for Si, Al, Na and K; synthetic oxides for Ti, Mn and Cr.

For volatile analysis, we used a 15 kV accelerating voltage, 60.0 nA current and a beam defocused to 10 μm. Peak/background count times were 60 s/30 s for sulphur and chlorine, and 120 s/60 s for fluorine. The calibration standards used were Elba Pyrite for sulphur and VG-568 for chlorine. For fluorine, we followed the method of Zhang et al. (2016), with X-Rays counted on a synthetic bilayer refracting crystal (LDE1), peak height analysis (PHA) settings chosen to remove interference with the Mg-Kβ peak, and a calibration curve established to accomodate interference between the F-Kα and Fe-Lα peaks. The suite of F-free, Fe-bearing primary glass standards required for calibration, and suite of F-bearing, Fe-bearing secondary glass standards required for verification of analytical precision, were synthesized and generously provided by C. Zhang, and are described in Zhang et al. (2016). Detection limits were 9 ppm, 19 ppm and between 100 and 120 ppm for S, Cl and F respectively (Schipper et al., 2019).

Both major and volatile analyses were regularly checked against a suite of natural and synthetic secondary standard reference glasses. For each sample, we performed multiple spot analyses. We then

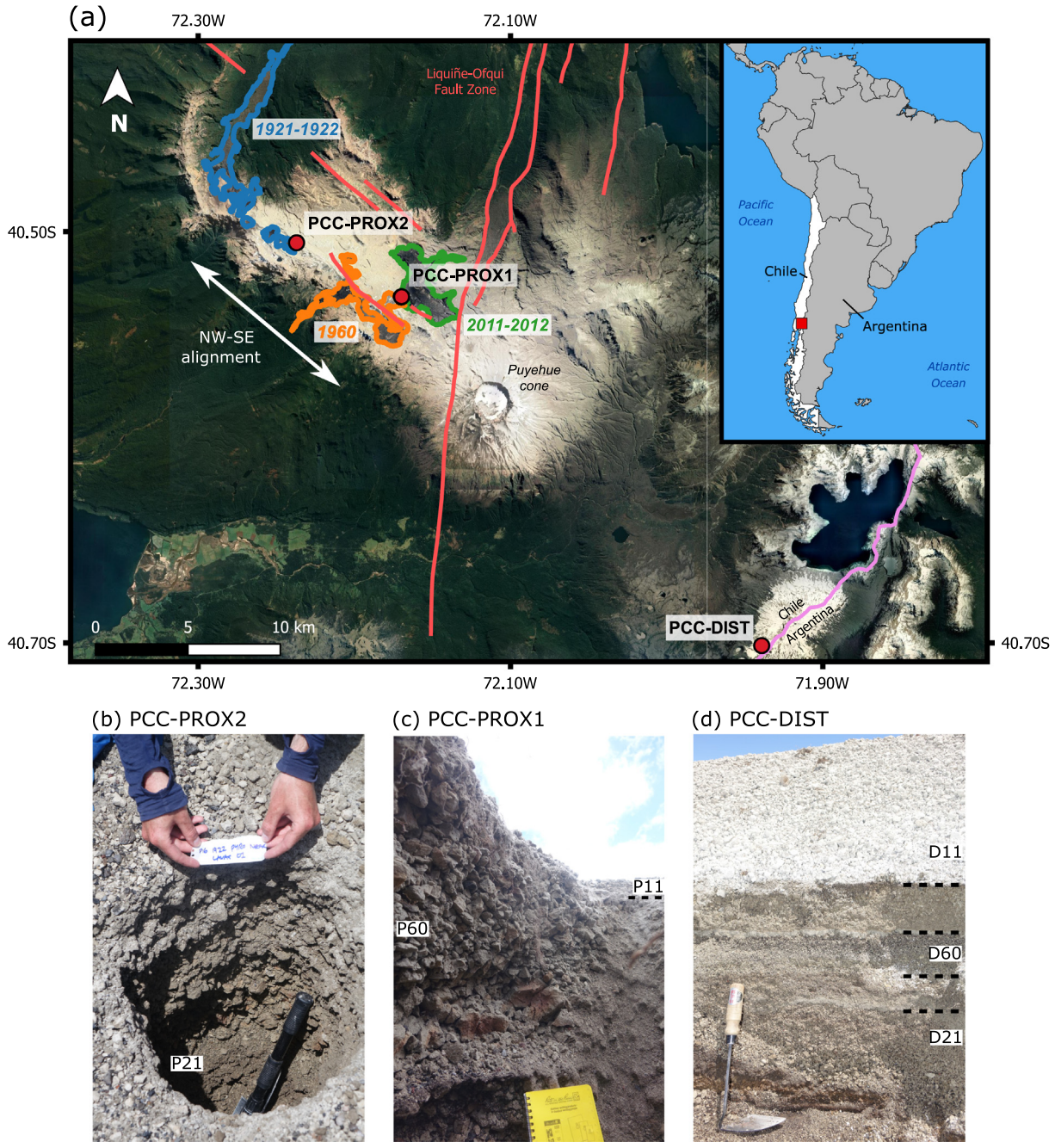

Fig. 1. (a) Satellite image (Google Satellite) of the Puyehue-Cordón Caulle Volcanic Complex. Lava flows are outlined for each of the three eruptions: 1921–1922 (blue), 1960 (orange) and 2011–2012 (green). Sample collection locations are shown as red dots. Fault locations are from Maldonado et al. (2021). Inset map shows location of the PCCVC in South America. (b, c, d) Photographs of the sampling locations. Proximal samples from the 1921–1922 eruption (P21) were collected at location PCC-PROX2 (b). Proximal samples from the 1960 (P60) and 2011–2012 (P11) eruptions were collected at location PCC-PROX1 (c). Distal samples for all three eruptions (D21, D60 and D11) were collected at location PCC-DIST (d). (For interpretation of the references to color in this figure legend, the reader is referred to the web version of this article.)

averaged the analyses with totals >97 wt.% to obtain the sample's composition.

3.3. Geobarometry

We used rhyolite-MELTS phase equilibria geobarometry with the Microsoft Excel interface for rhyolite-MELTS (Gualda and Ghiorso, 2014, 2015) to estimate the storage and extraction pressures of the magmas erupted at Cordón Caulle in 1921–1922, 1960 and 2011–2012. This geobarometry technique uses rhyolite-MELTS (v1.0.x; Gualda et al., 2012) to simulate equilibrium crystallisation of a melt with a given major element composition for a range of pressures and temperatures. It returns the pressure at which the input melt composition can be in equilibrium with a given mineral assemblage.

To model storage pressures, the input compositions used are matrix glass compositions. We assume that the glass represents the melt that was stored in equilibrium with the given phenocryst assemblage immediately prior to eruption (Gualda and Ghiorso, 2014), which is supported by the absence of visible microlites our samples (Fig. 2). The eruptive products from Cordón Caulle are crystal-poor (<5% phenocrysts), but the most abundant mineral phases are (see Gerlach et al., 1988; Castro et al., 2013; Jay et al., 2014): plagioclase (plag),

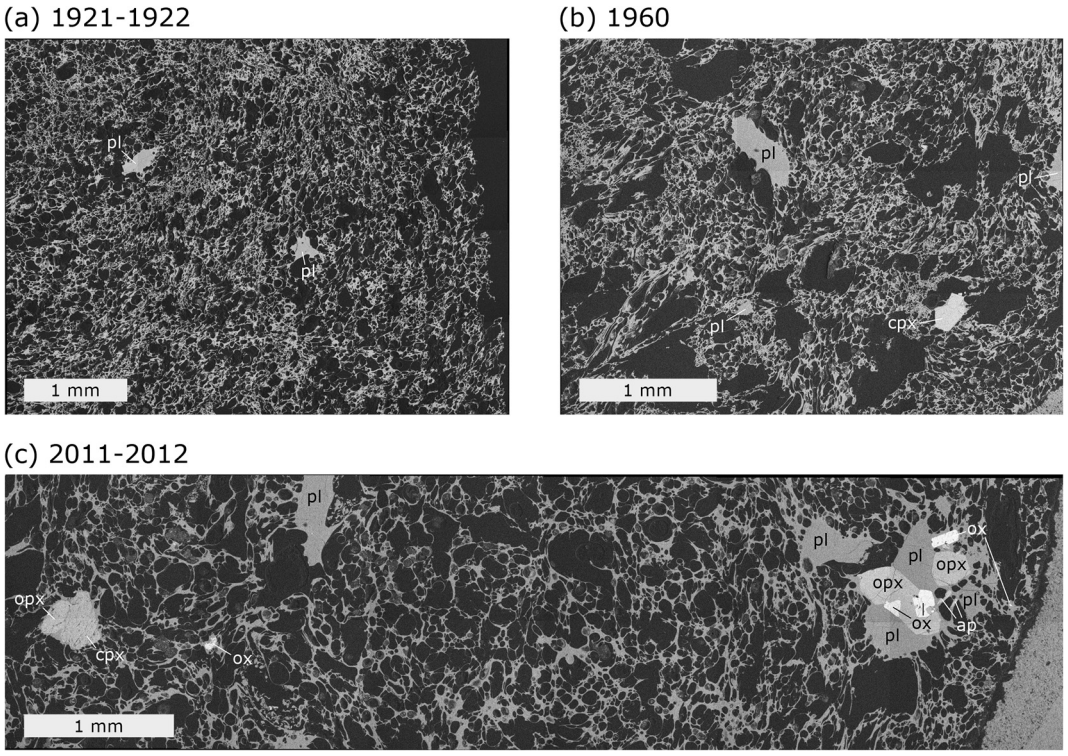

Fig. 2. Representative BSE images of thin sections of Cordón Caulle pumice lapilli from (a) the 1921–1922 eruption (sample P21_78), (b) the 1960 eruption (sample P60_04), and (c) the 2011–2012 eruption (sample P11_61). Phenocrysts are either isolated or form glomerocrysts. The groundmass glass is devoid of microlites. Mineral symbols ap = apatite, cpx = clinopyroxene, opx = orthopyroxene, ox = Fe-Ti oxide, pl = plagioclase.

Table 1
Matrix glass major element and volatile compositions as determined by EPMA, from pyroclasts of the 1921–1922, 1960 and 2011–2012 eruptions at Cordón Caulle. For each sample, the first line represents the averages of *n* spot analyses and the second line (italics font) corresponds to the standard deviations. These data, along with analyses of standard glasses are available as Supplementary Material.

Sample name	Eruption	SiO_2	TiO_2	Al_2O_3	FeO_t	MnO	MgO	CaO	Na_2O	K_2O	Cr_2O_3	S (ppm)	F (ppm)	Cl (ppm)	Total	*n*
P21_10	1921–1922	68.38	0.82	14.98	4.07	0.12	0.93	2.86	4.59	2.40	0.00	–	–	–	99.15	40
		0.29	*0.04*	*0.08*	*0.15*	*0.02*	*0.03*	*0.05*	*0.13*	*0.17*	*0.01*					
P21_15	1921–1922	68.13	0.81	14.91	4.08	0.12	0.91	2.77	4.94	2.28	0.01	–	–	–	98.95	30
		0.40	*0.04*	*0.25*	*0.22*	*0.02*	*0.05*	*0.15*	*0.20*	*0.30*	*0.01*					
P21_43	1921–1922	67.92	0.73	14.69	3.77	0.12	0.82	2.64	4.62	2.39	0.01	40	1060	1959	98.02	9
		0.58	*0.02*	*0.18*	*0.22*	*0.02*	*0.02*	*0.04*	*0.14*	*0.27*	*0.01*	*19*	*144*	*836*		
P21_47	1921–1922	68.55	0.81	14.91	4.04	0.12	0.87	2.76	4.70	2.46	0.01	50	922	1594	99.50	20
		0.32	*0.03*	*0.11*	*0.15*	*0.02*	*0.03*	*0.06*	*0.12*	*0.17*	*0.01*	*14*	*53*	*61*		
P21_70	1921–1922	68.22	0.82	14.97	4.10	0.12	0.93	2.85	5.04	2.41	0.01	–	–	–	99.47	21
		0.34	*0.03*	*0.09*	*0.17*	*0.02*	*0.02*	*0.06*	*0.13*	*0.16*	*0.01*					
P21_78	1921–1922	69.49	0.73	14.83	3.74	0.12	0.76	2.52	4.57	2.56	0.01	–	–	–	99.33	42
		0.30	*0.03*	*0.10*	*0.13*	*0.02*	*0.03*	*0.08*	*0.12*	*0.13*	*0.01*					
P21_91	1921–1922	67.17	0.76	14.66	3.83	0.12	0.84	2.63	4.99	2.23	0.01	–	–	–	97.25	14
		0.28	*0.04*	*0.34*	*0.14*	*0.02*	*0.05*	*0.16*	*0.21*	*0.22*	*0.01*					
D21_14	1921–1922	68.73	0.82	15.05	4.01	0.12	0.89	2.84	4.56	2.42	0.01	–	–	–	99.46	42
		0.27	*0.04*	*0.13*	*0.12*	*0.02*	*0.04*	*0.07*	*0.11*	*0.19*	*0.01*					
D21_99	1921–1922	68.20	0.77	14.96	3.90	0.10	0.86	2.75	4.85	2.49	0.01	49	874	1569	99.14	11
		0.41	*0.03*	*0.09*	*0.31*	*0.02*	*0.04*	*0.08*	*0.14*	*0.08*	*0.02*	*10*	*163*	*227*		
P60_04	1960	70.22	0.54	14.33	3.18	0.10	0.52	1.99	4.85	2.81	0.01	–	–	–	98.55	23
		0.37	*0.02*	*0.11*	*0.22*	*0.02*	*0.02*	*0.06*	*0.16*	*0.07*	*0.02*					
P60_24	1960	70.70	0.55	14.40	3.16	0.10	0.50	1.94	4.88	2.81	0.01	48	960	1703	99.32	27
		0.45	*0.02*	*0.13*	*0.17*	*0.02*	*0.02*	*0.05*	*0.10*	*0.07*	*0.01*	*21*	*68*	*92*		
P60_39	1960	70.75	0.49	14.10	2.98	0.10	0.44	1.78	4.84	2.92	0.01	–	–	–	98.41	18
		0.45	*0.02*	*0.13*	*0.23*	*0.02*	*0.03*	*0.05*	*0.15*	*0.06*	*0.01*					
P60_74	1960	70.48	0.53	14.34	3.04	0.10	0.49	1.89	4.65	2.81	0.01	32	1042	1607	98.60	39
		0.36	*0.02*	*0.14*	*0.16*	*0.02*	*0.03*	*0.07*	*0.13*	*0.12*	*0.01*	*15*	*108*	*113*		
D60_17	1960	71.10	0.53	14.35	2.94	0.09	0.47	1.86	4.58	2.86	0.00	22	986	1699	99.05	18
		0.34	*0.02*	*0.09*	*0.17*	*0.02*	*0.02*	*0.03*	*0.34*	*0.05*	*0.01*	*10*	*54*	*77*		
D60_19	1960	70.03	0.48	14.17	2.73	0.10	0.44	1.76	4.59	2.73	0.00	42	951	1945	98.21	9
		0.70	*0.02*	*0.23*	*0.15*	*0.02*	*0.02*	*0.03*	*0.15*	*0.19*	*0.01*	*17*	*98*	*234*		
P11_61	2011–2012	69.98	0.51	14.29	2.92	0.09	0.47	1.83	4.79	2.76	0.01	28	1014	1610	97.92	14
		0.41	*0.03*	*0.11*	*0.20*	*0.02*	*0.03*	*0.08*	*0.09*	*0.19*	*0.01*	*15*	*139*	*247*		
P11_73	2011–2012	70.54	0.55	14.38	3.14	0.10	0.49	1.93	4.75	2.81	0.00	32	992	1548	98.95	28
		0.35	*0.03*	*0.10*	*0.15*	*0.02*	*0.02*	*0.09*	*0.11*	*0.04*	*0.01*	*17*	*59*	*98*		

orthopyroxene (opx) and clinopyroxene (cpx). We considered the mineral assemblage plag + opx, following the method of Harmon et al. (2018). While our samples do contain cpx, rhyolite-MELTS is not calibrated for cpx in melts with high SiO_2 contents due to the absence of cpx-liquid phase equilibria in rhyolitic melt in the calibration database (Ghiorso, pers. comm.). The absence of cpx is expected to make minimal difference to the results (Harmon et al., 2018), although the plag + opx pressure calculations will have larger uncertainties than a plag + opx + cpx geobarometry calculation. We calculated storage pressure for a total of 22 glass compositions: nine from the 1921–1922 eruption (this study), six from the 1960 eruption (this study) and seven from the 2011–2012 eruption (two from this study and five measured by Schipper et al., 2019).

Following the procedure of Harmon et al. (2018), we ran the compositions through rhyolite-MELTS from 400 to 25 MPa in 25 MPa steps and from 1100 to 700 °C in 1 °C steps. We assumed that the melt was water saturated at all pressures. For consistency, we used 10 wt.% H_2O to force water saturation at all pressures (following Harmon et al., 2018). Melt inclusions from the 2011–2012 eruptions indicate that the melt also contained dissolved CO_2 in its pre-eruption storage (up to 220 ppm; Castro et al., 2013; Jay et al., 2014). The effect of CO_2 is not explicitly modelled in the rhyolite-MELTS geobarometer but is assumed to have a minor impact on the pressure calculations (Gualda and Ghiorso, 2014; Ghiorso and Gualda, 2015). The resulting pressures are sensitive to the choice of oxygen fugacity (fO_2; Harmon et al., 2018). fO_2 values have previously been estimated for all three eruptions using magnetite-ilmenite pairs. With respect to the Ni-Ni oxide (NNO) buffer they are approximately NNO-0.3 for the 1921–1922 eruption (Gerlach et al., 1988; Mingo, 2019), NNO-0.5 for the 1960 eruption (Gerlach et al., 1988; Mingo, 2019) and NNO-0.8 for the 2011–2012 eruption (Castro et al., 2013; Jay et al., 2014; Mingo, 2019). We thus considered a range of five fO_2 values from NNO-1 to NNO in 0.25 ΔNNO increments, in order to fully explore the expected fO_2 range.

In addition to the storage pressure, rhyolite-MELTS geobarometry can assess the extraction pressure. The extraction pressure is the pressure at which the melt segregated from its parental mush (Gualda et al., 2019). The procedure was identical to the storage pressure calculations described above, with the exception that we used bulk composition as the initial input (as opposed to matrix glass composition used previously). The underlying hypothesis is that pure melt (0% crystal) was first extracted from a parental mush at the extraction pressure, and subsequently crystallised at the storage pressure to become the

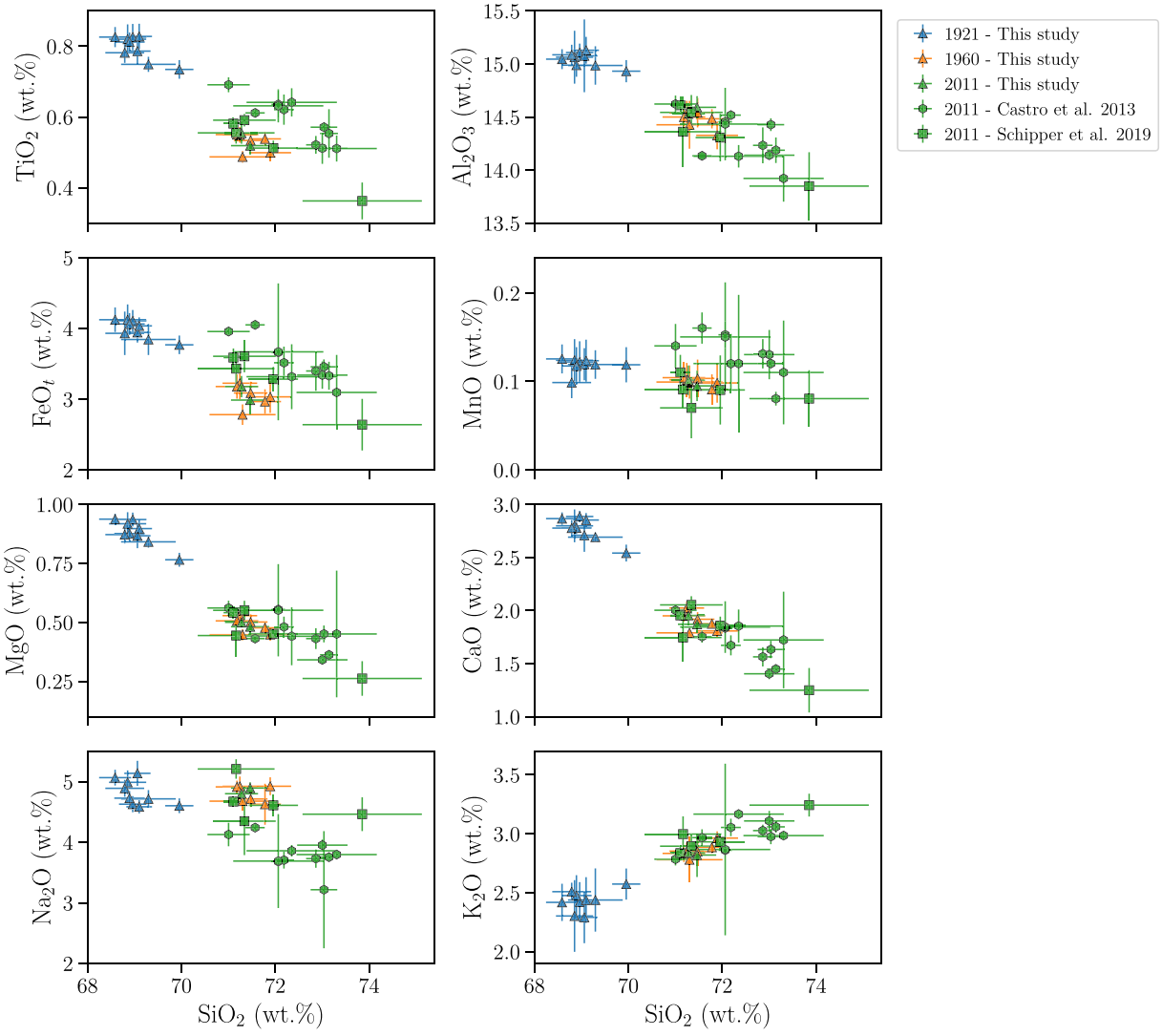

Fig. 3. Harker diagrams showing major element compositions of matrix glass from pyroclasts of the 1921–1922 (blue), 1960 (orange) and 2011–2012 (green) eruptions at Cordón Caulle. Major elements are normalised to 100%, volatile-free. Each point represents the average of multiple spots analyses (n = 9–42), error bars represent ±1 standard deviation. (For interpretation of the references to color in this figure legend, the reader is referred to the web version of this article.)

final assemblage of melt and crystals that we observe at the surface. Assuming perfect extraction and closed system crystallisation, the erupted bulk composition should be identical to the extracted melt composition (Gualda et al., 2019). We considered a plag + opx assemblage again. Bulk compositions were collated from published literature, all were acquired via X-ray fluorescence (XRF). We ran a total of 38 published bulk compositions: six from the 1921–1922 eruption (Gerlach et al., 1988; Singer et al., 2008; Naranjo et al., 2017), nine from the 1960 eruption (Gerlach et al., 1988; Singer et al., 2008) and 23 from the 2011–2012 eruption (Castro et al., 2013; Jay et al., 2014; Naranjo et al., 2017; Schipper et al., 2019).

4. Results

4.1. Geochemical analysis

Major element compositions of the matrix glass for the 1921–1922, 1960 and 2011–2012 eruptions are presented in Table 1 and Harker diagrams in Fig. 3. Each sample composition results from averaging between nine and 42 spot analyses, with a mean number of 24 spot analyses per sample. Previously published matrix glass compositions from pumice clasts from the 2011–2012 eruption (Castro et al., 2013; Schipper et al., 2019) are also displayed in Fig. 3 for comparison. Abundances of TiO_2, Al_2O_3, FeO_t, MgO, CaO and Na_2O all decrease with increasing SiO_2 content, whereas K_2O shows an increasing trend. Matrix glasses from the 1960 and 2011–2012 eruptions are chemically homogeneous and indistinguishable, with normalized average SiO_2 values of 71.5 wt.% and 72.2 wt.%, respectively. Matrix glasses from the 1921–1922 samples are chemically homogeneous but form a distinct sub-population in Fig. 3, with lower SiO_2 content (normalized average of 69.0 wt.%), lower K_2O content, similar to higher Na_2O content, and higher CaO, Al_2O_3, FeO_t, MgO and TiO_2 contents than their 1960 and 2011–2012 counterparts.

Volatile contents for pyroclasts from the 1921–1922, 1960 and 2011–2012 eruptions are presented in Fig. 4, along with published data from Schipper et al. (2019) from the 2011–2012 eruption. Matrix glasses from all three eruptions contained similar sulphur, fluorine and chlorine contents, despite different SiO_2 contents. Our data also overlap published data, with low S values and high F and Cl. This is consistent with observations from Schipper et al. (2019) that halogens remain dissolved in the melt for low groundmass microlite contents (<75%).

4.2. Rhyolite-MELTS geobarometry

All 110 simulations for the glass compositions (five fO_2 values for 22 compositions) returned a plag + opx solution. For each data point, the 1σ uncertainty associated with storage pressure calculations using rhyolite-MELTS is on the order of 25 MPa (Harmon et al., 2018), mainly deriving from analytical error in the input glass composition (Gualda and Ghiorso, 2014; Harmon et al., 2018). The storage pressure estimates for each of the eruptions are displayed as histograms in Fig. 5. fO_2 exerts a significant control on estimated storage pressures, with higher fO_2 values yielding higher (i.e. deeper) storage pressures. Reported fO_2 values for each of the three eruptions show a decreasing trend from NNO-0.3 in 1921–1922 to NNO-0.8 in 2011–2012 (Gerlach et al., 1988; Castro et al., 2013; Jay et al., 2014; Mingo, 2019). We restrict our attention to the rhyolite-MELTS runs with fO_2 values most closely matching these estimates, i.e. −0.25 for 1921–1922, −0.5 for 1960 and −0.75 for 2011–2012 (Fig. 6). The corresponding storage pressure ranges are 90–112 MPa for the 1921–1922 eruption, 123–143 MPa for the 1960 eruption and 79–146 MPa for the 2011–2012 eruption. Overall, storage pressures for all three eruptions lie in the range 80–150 MPa. The 1921–1922 storage pressures are ~30 MPa lower than the 1960 ones and the 2011–2012 results encompass both the 1921–1922 and 1960 pressure ranges. We tested whether the 30 MPa difference

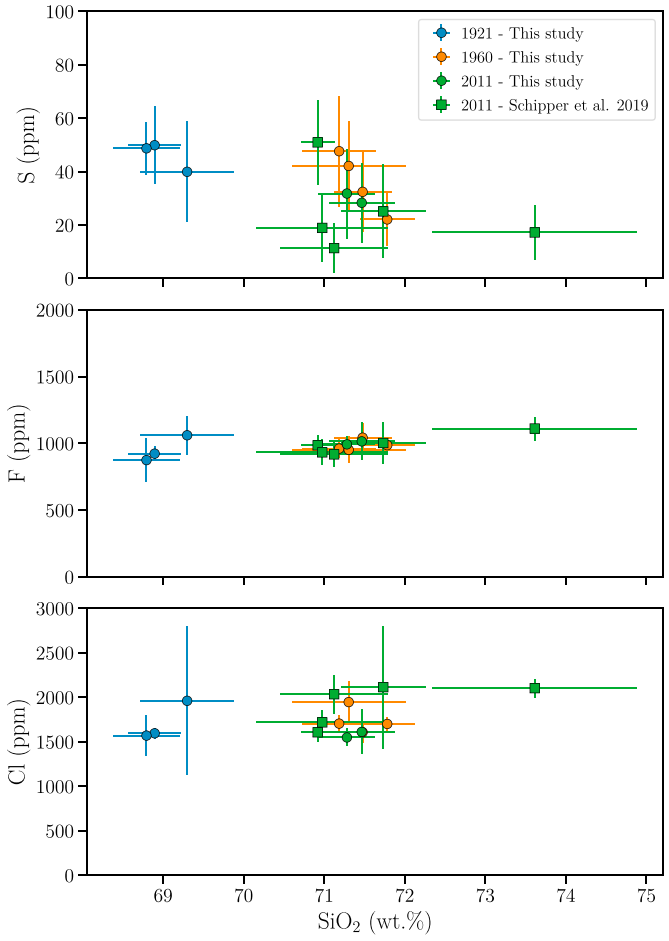

Fig. 4. Volatiles versus SiO_2 for selected samples from the 1921–1922 (blue), 1960 (orange) and 2011–2012 (green) eruptions at Cordón Caulle. Each point represents the average of multiple spots analyses (n = 9–42), error bars represent ±1 standard deviation. (For interpretation of the references to color in this figure legend, the reader is referred to the web version of this article.)

in storage pressures between the 1921–1922 and 1960 eruptions could have occurred by chance due to our small sample sizes by performing a Welch's unequal variances t-test. We obtained a t-score of 7.5 and a p-value of 4×10^{-5}, suggesting that there is <0.004% chance that the 1921–1922 and 1960 data have the same mean.

All 190 simulations for the bulk compositions (five fO_2 values for 38 compositions) yielded a successful plag + opx extraction pressure estimate (Fig. 5). For every fO_2 value, the extraction pressures overlap with the storage pressures, and generally extend to higher pressures, with a mode ~50 MPa higher on average (Fig. 5). Oxygen fugacity exerts a strong control on the estimated extraction pressures too, with a change of 1 log unit in fO_2 leading to variations up to 150 MPa in pressures. If we consider the estimated fO_2 values for each eruption, we obtain extraction pressures of 111–192 MPa for 1921–1922, 113–203 MPa for 1960 and 70–163 MPa for 2011–2012 (Fig. 6). Thus the extraction pressures are similar for all three eruptions, broadly falling in the range 70–200 MPa.

5. Discussion

5.1. Magma storage at Cordón Caulle

The rhyolite-MELTS geobarometer indicates that magma was stored at pressures between 80–150 MPa for all three eruptions (Fig. 6). Using an average crustal density of 2300 kg · m^{-3} (e.g. Castro et al., 2013), this

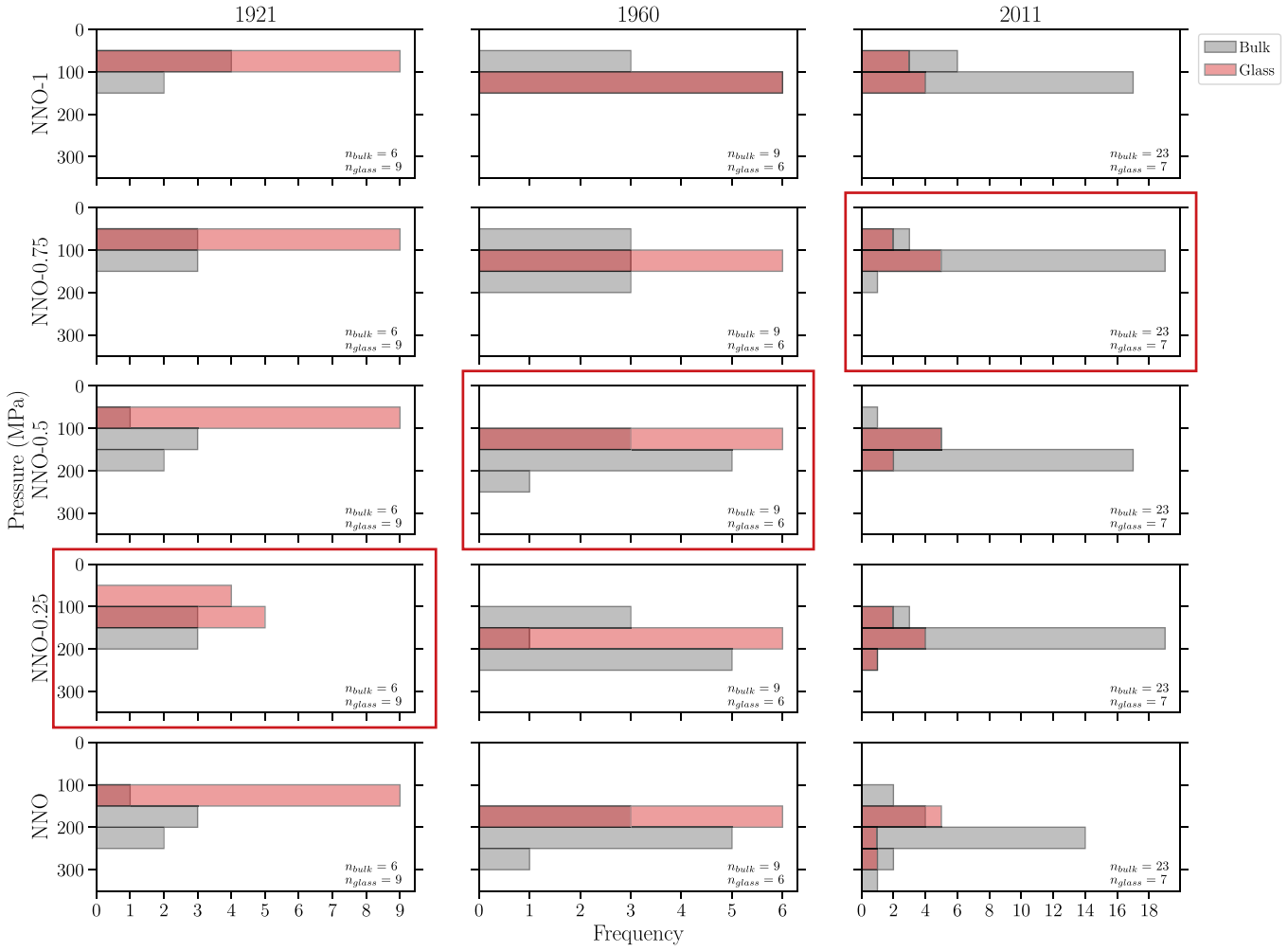

Fig. 5. Rhyolite-MELTS geobarometry results. Glass compositions (red) give storage pressures whereas bulk compositions (grey) yield extraction pressures. The red boxes indicate our best-estimate of storage and extraction pressures using independent fO_2 data, and are reproduced as boxplots in Fig. 6. (For interpretation of the references to color in this figure legend, the reader is referred to the web version of this article.)

corresponds to depths of 3.5–6.6 km, i.e. the shallow crust. Storage pressure for the 2011–2012 has been independently estimated using petrological experiments (50–115 MPa, Castro et al., 2013) and H_2O-CO_2 equilibria of melt inclusions (100–140 MPa, Jay et al., 2014). Additionally, InSAR data reveal co-eruptive deflation sources at depths 4–6 km (i.e. 90–135 MPa, Jay et al., 2014; Wendt et al., 2017; Delgado et al., 2019). All of these independent estimates (overall 50–140 MPa) are in agreement with our rhyolite-MELTS results for 2011–2012 (79–146 MPa). The consistency between rhyolite-MELTS and other independent geobarometers for the 2011–2012 case bolsters the validity of the results for 1921–1922 and 1960.

Magma storage for the 1921–1922 and 1960 eruptions was hitherto assumed to be at similar depths to that of the 2011–2012 magma body (i.e. 50–140 MPa), solely based on geochemical similarity (Jay et al., 2014; Delgado et al., 2018). Our results constitute the first direct test of this hypothesis and allow us to both validate and refine it. Indeed, magma was stored at pressures within the range 50–140 MPa in 1921–1922 and 1960, but the storage regions for these two eruptions were confined to narrower pressure ranges that are distinct and do not overlap (Fig. 6). The 1921–1922 storage region was shallower, between 90–112 MPa (4.0–5.0 km) whereas the 1960 storage region was slightly deeper, at 123–143 MPa (5.4–6.3 km). The tight clustering of storage pressures gives us confidence in the significance of the relative difference between these two events. This is further supported by a Welch's *t*-test with a *t*-score of 7.5 and a *p*-value <.001, allowing us to reject the null hypothesis that the two datasets have the same mean. Nonetheless, both ranges are within the larger range of storage pressures estimated for the 2011–2012 eruption (79–146 MPa). The larger pressure range for the 2011–2012 eruption may reflect a larger, more vertically extensive magma reservoir, which is consistent with the ~10 times larger erupted volume. Additionally, it may reflect a more complex reservoir structure, with two or three distinct high melt-fraction pockets (Alloway et al., 2015; Coppola et al., 2017; Wendt et al., 2017).

5.2. Magma factory at Cordón Caulle

Modern views of silicic magmatic systems envisage crystal-rich mush zones from which eruptible melt segregates and accumulates into shallower ephemeral magma chambers (e.g. Bachmann and Huber, 2016; Cashman et al., 2017; Sparks et al., 2019). A corollary question is how far apart in space do extraction and storage occur? Melt extraction and melt storage are generally thought to occur at similar depths (e.g. Bachmann and Bergantz, 2008; Foley et al., 2020), but recent evidence suggests that melt may be transported over great vertical distances (>10 km) between extraction and storage (e.g. Gualda et al., 2019; Pitcher et al., 2020). The rhyolite-MELTS geobarometer allows the extraction and storage pressures to be estimated independently with the same method (Gualda et al., 2019; Foley et al., 2020; Pitcher et al., 2020; Pamukçu et al., 2020). Overall, extraction occurred at

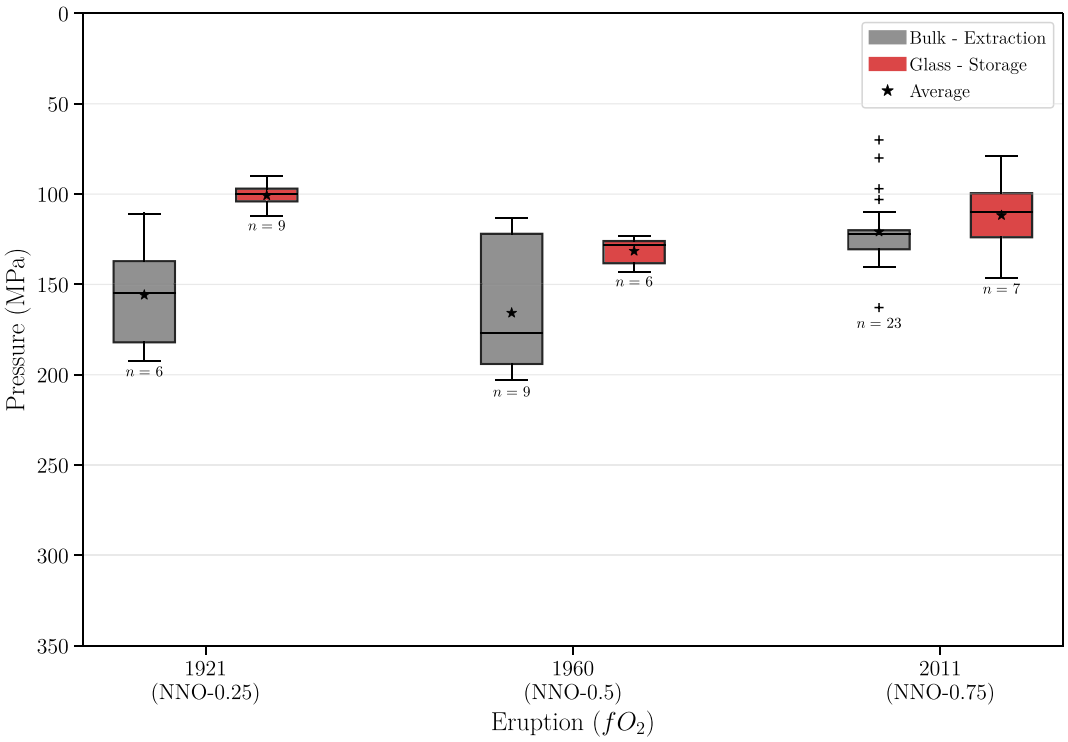

Fig. 6. Boxplot of the rhyolite-MELTS geobarometry results for fO_2 values closest to independently measured values. Storage pressures are in red, extraction pressures are in grey. Boxes are drawn from the first to the third quartile, with the median shown as a black line and the average as a black star. Whiskers extend to the last point falling within 1.5 interquartile range (i.e. whiskers do not represent uncertainty), all other points are plotted as crosses. (For interpretation of the references to color in this figure legend, the reader is referred to the web version of this article.)

pressures in the range 70–203 MPa (3.1–9.0 km). This extraction range overlaps with the ranges of storage pressures for all three eruptions and extends deeper into the crust (Fig. 6). This suggests extraction and storage occurred contiguously: melt is extracted throughout the mush and stored in high melt-fraction pockets in the shallower part of the mush, or just above it. Overall, our results indicate that, both extraction and storage occurred in the shallow crust (<10 km depth) for the last three eruptions at Cordón Caulle. These new data bring additional constraints to our understanding of the architecture of silicic systems, as transcrustal and/or translateral systems (e.g. Kennedy et al., 2018; Biggs and Annen, 2019; Sparks et al., 2019; Delgado, 2021).

Current models for the magmatic system operating beneath Cordón Caulle comprise a crystal-rich mush zone between 4 and 9 km depth, with a considerable lateral extent from Cordillera-Nevada to the NW to Puyehue cone to the SE (~20 km, Jay et al., 2014; Delgado, 2021). The magmas erupted in the three historical eruptions (1921–1922, 1960 and 2011–2012) would then all be sourced from this single more crystalline region. Our extraction depths (3.1–9.0 km) reinforce this model. The mush is likely to be composed primarily of mafic minerals (i.e. a dioritic assemblage). This assumption is based on the absence of quartz in Cordón Caulle products and the presence of mafic glomerocrysts in the deposits (Fig. 2; Jay et al., 2014). Melt was produced in a unique, extensive crystal-mush region for all three eruptions, but we suggest that the magma chambers were discrete, both in space and time. Each chamber was located at slightly different depths (Fig. 6), and perhaps at different lateral positions within the mush (based upon vent locations, Fig. 1). We now describe the life cycle of silicic melt at Cordón Caulle, from production to eruption, and in light of our geobarometry results (Fig. 7).

Melt first segregates from the mush at 4–9 km depth. The actual segregation mechanism is beyond the scope of our study but current models on silicic melt extraction offer a range of possible processes (e.g. Sparks et al., 2019; Edmonds et al., 2019): gravitationally-driven compaction, gas filter-pressing, rejuvenation by magma recharge or external stresses. The timescales associated with these mechanisms vary from a few weeks to a few thousand years (Cooper, 2019). Extracted melt is buoyant in the mush region and will thus migrate upwards if possible. Resolving the exact transport processes occurring at Cordón Caulle is beyond the scope of this contribution, but we posit that it most likely includes upward transport via porous flow, Rayleigh-Taylor instabilities or dykes (Sparks et al., 2019). Segregated melt is thus transported to the top of the mush where it accumulates to potentially form magma chambers, that may or may not be interconnected. These magma chambers are located at depths between 3.5 and 6.6 km, according to our storage pressure estimates, and in agreement with the depths of source models inverted from InSAR data (e.g. Delgado, 2021). The shallower the depth, the more volatiles exsolve out of the melt (mainly H_2O, CO_2 and S; Castro et al., 2013; Jay et al., 2014; Schipper et al., 2019). Vesiculation increases both the buoyancy and pressurisation within the magma chamber. Simultaneously, melt cools and crystallises in the magma chamber. If the pressurisation is sufficient to rupture the overlying country rock, dykes will form and magma is erupted at the surface as fissure eruptions (e.g. Tramontano et al., 2017; Kavanagh, 2018), as observed with the three events considered here.

5.3. Seismic-triggering at Cordón Caulle

One of the key objectives of our study is to investigate possible seismic-triggering mechanisms at Cordón Caulle. The 1921–1922 eruption was not preceded by any significant tectonic earthquake, and as such is considered to have occurred under "normal" stress conditions (Lara et al., 2004). Hence, the 1921–1922 eruption can be considered our control eruption. The 1960 eruption occurred 38 hours and <100 km from the May 22 1960 Great Chilean (Valdivia) earthquake (M_w9.5), hence raising the question of whether the eruption was triggered by the earthquake (Barrientos, 1994; Lara et al., 2004;

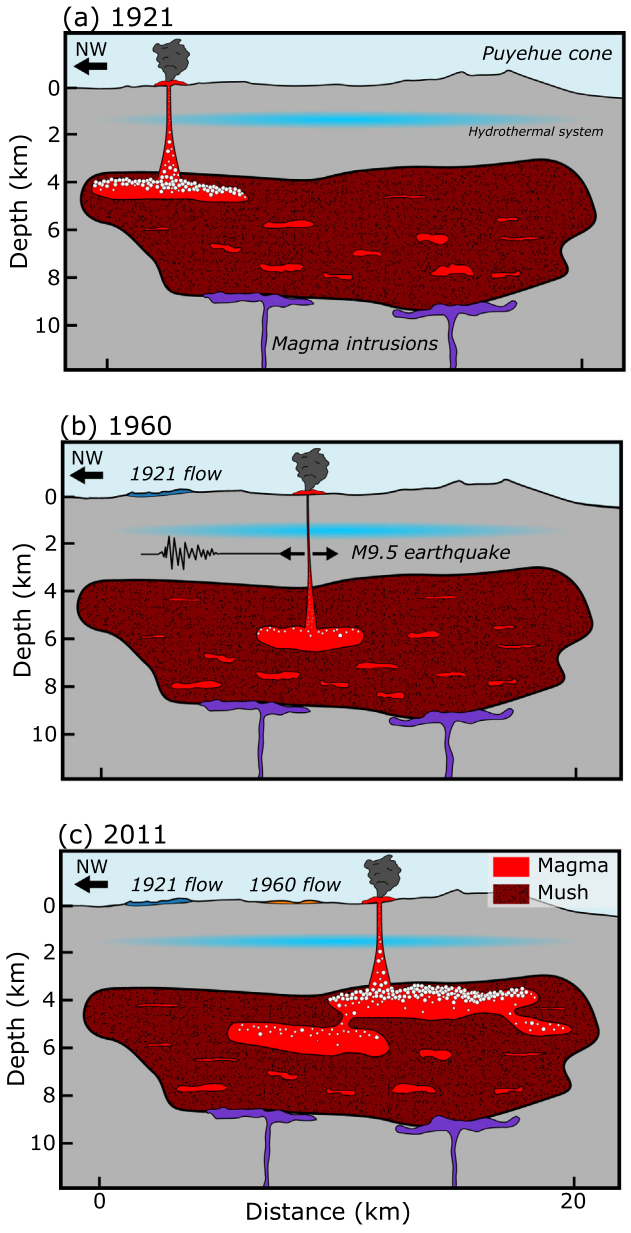

Fig. 7. Cartoon cross-section showing the time evolution of the magmatic system operating beneath the Puyehue-Cordón Caulle Volcanic Complex, inspired by Jay et al. (2014), Delgado et al. (2016) and Delgado et al. (2018). The dark red region with black spots represents the dioritic crystal mush, whereas the bright red regions depict eruptible magma. The amounts of bubbles are schematics and represent the amount exsolved of volatiles in the magmas at the onset of eruption. The purple regions represent periodic magma intrusions (Jay et al., 2014; Delgado et al., 2016, 2018). The actual shape of the magma bodies and the crystal mush are hypothetical, as there are no detailed geophysical data for this volcanic centre. (For interpretation of the references to color in this figure legend, the reader is referred to the web version of this article.)

Walter and Amelung, 2007; Watt et al., 2009; Bonali et al., 2013). The Great Chilean earthquake itself was the culmination of a complex series of large foreshocks (up to M_w8.1 for the May 21 Concepción earthquake; e.g. Cifuentes, 1989; Ojeda et al., 2020). Whether Cordón Caulle responded to the M_w9.5 Valdivia event only or to the entire sequence of events lies beyond the scope of this study. A similar much weaker association has also been assessed for the 2011–2012 eruption and the M_w8.8 Maule earthquake that occurred 16 months earlier (Bonali et al., 2013; Jay et al., 2014).

In 1960, the stress field changes resulting from the earthquake sequence on the magmatic system were extreme due to the magnitude and proximity to the rupture zone (Barrientos, 1994; Walter and Amelung, 2007; Moreno et al., 2009; Bonali et al., 2013). In particular, the magmatic system experienced "unclamping" (i.e. extension) which reduces confining pressure and can facilitate dyke propagation to the surface (e.g. Bonali et al., 2013; Seropian et al., 2021). Unclamping has been reported to "advance the clock" to an already impending eruption (e.g. Walter and Amelung, 2006; Walter, 2007; Chesley et al., 2012; Caricchi et al., 2021) or to initiate eruption of high-crystallinity, low-volatiles, underpressurised magmas that would otherwise be uneruptible (La Femina et al., 2004). The 1960 pyroclasts contain few crystals (Fig. 2) and our new data indicate that they are geochemically very similar to the other eruptions (Figs. 3 and 4), suggesting that the magma was eruptible prior to the earthquake. This is consistent with an advance-clock mechanism: an eruption might have occurred at Cordón Caulle regardless, but the earthquake brought it forward in time. Furthermore, the presence of an active hydrothermal system at Cordón Caulle (Sepúlveda et al., 2004) increases the potential of this volcanic centre to be seismically-triggered, especially if it was already in a heightened state of unrest (Seropian et al., 2021). Unfortunately, no monitoring data exist that could indicate the state of Cordón Caulle before the 1960 earthquake, to assess whether it was already in a heightened state of unrest.

Our geobarometry data indicate that the 1960 magma body was stored ~1.3 km (30 MPa) deeper than the 1921–1922 one (Fig. 6). A direct implication of this result concerns the amount of dissolved volatiles in the melt, and thereby the amount of exsolved volatiles in the magma chamber. Assuming saturation, the amount of dissolved volatiles (mainly H_2O and CO_2) scales with pressure (e.g. Baker and Alletti, 2012). We computed the concentration of dissolved water at the top of the 1921–1922 and 1960 magma storage regions (i.e. at pressures of 90 and 123 MPa respectively, Fig. 8) using VESIcal (v. 0.9.10; Iacovino et al., in press) with the model of Ghiorso and Gualda (2015). In addition to pressure, the calculations require prior knowledge of the temperature and the mole fraction of H_2O in the H_2O-CO_2 fluid X_{H_2O}. Storage temperatures for the 1921–1922 and 1960 eruptions were estimated by Gerlach et al. (1988) as 975 °C and 915 °C, respectively, both with a ±50 °C uncertainty. The initial volatile content, and thus X_{H_2O}, is unknown for the 1921–1922 and 1960 magmas. In general, for a silicic melt at pressures <200 MPa, X_{H_2O}>0.5 (Baker and Alletti, 2012) thus we performed the calculations for a range of X_{H_2O} from 0.5 to 1. The 1960 melt contained between 0.42 and 0.93 wt.% more dissolved water than the 1921–1922 melt (for X_{H_2O} of 0.5 and 1, respectively, Fig. 8). Consequently, the 1960 magma likely contained less exsolved volatiles than the 1921–1922 magma. With less exsolved volatiles, the 1960 magma may have been less likely to develop the necessary overpressures to erupt without the aid of the

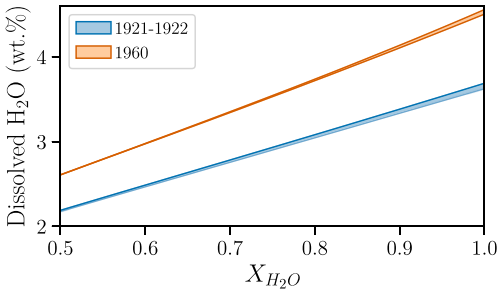

Fig. 8. Dissolved water content in the melt (in wt.%) as a function of mole fraction of water in the fluid X_{H_2O} for the 1921–1922 and 1960 magmas. Calculations were performed using VESIcal (v. 0.9.10; Iacovino et al., in press) with the "MagmaSat" model of Ghiorso and Gualda (2015). For the 1921–1922 case (blue), we used a pressure of 90 MPa and temperatures of 925 °C (top blue line) and 1025 °C (bottom blue line). For the 1960 case (orange), we used a pressure of 123 MPa and temperatures of 865 °C (top orange line) and 965°C (bottom orange line). (For interpretation of the references to color in this figure legend, the reader is referred to the web version of this article.)

earthquake. Hence, by reducing the necessary stresses to open a conduit, the 1960 Great Chilean earthquake allowed the ascent and extrusion of a magma that was rheologically eruptible, but perhaps not sufficiently overpressurized yet.

Concerning the 2011–2012 eruption, the resulting stress changes from the 2010 Maule earthquake were much weaker than in 1960 (Bonali et al., 2013). The deformation rate of the volcano did not significantly vary following the earthquake (Jay et al., 2014; Delgado, 2021) and testing for a trigger via an unclamping mechanism was inconclusive (Bonali et al., 2013). However, the earthquake did trigger local hydrothermal activity (Jay et al., 2014). It is also possible that the shear stresses from the earthquake facilitated melt segregation and/or accumulation (e.g. Holtzman et al., 2003; Davis et al., 2007; Sumita and Manga, 2008), though it remains impossible to test rigorously with the currently available data.

6. Conclusion

Cordón Caulle in southern Chile produced three moderate dacitic to rhyolitic eruptions in the past century, in 1921–1922, 1960 and 2011–2012. Using new glass geochemical data and thermodynamic modelling we add new constraints to the architecture of the magmatic system that fed these three eruptions. The main results of our study are summarized as follows:

1. Matrix glass in the pyroclasts from the 1960 eruption is chemically indistinguishable from the glass in products erupted in 2011–2012. The glass from the products of the 1921–1922 eruption is noticeably less evolved.
2. Magma was stored in the shallow crust, at pressures between 80 and 150 MPa (3.5–6.6 km depth) for all three eruptions. The 1960 magma reservoir was slightly deeper (5.4–6.3 km) than the 1921–1922 one (4.0–5.0 km).
3. Melt extraction pressures are in the range 70–200 MPa (3.1–9.0 km depth) suggesting that melt segregated from a crystalline mush and was then stored either near the top within it or just above it. The same mush zone likely fed all three eruptions, indicating that the mush system is most likely longer lived than the individual eruptible magma bodies.
4. The 1960 magma was stored in a deeper reservoir than the 1921–1922 and 2011–2012 magmas. The stress changes resulting from M_w9.5 Great Chilean earthquake potentially promoted the beginning of an already approaching eruption.

Declaration of Competing Interest

The authors declare no conflict of interest.

Acknowledgements

We would like to thank Rob Spiers and Ulf Zinkernagel for their help preparing thin sections, Guilherme Gualda and Mark Ghiorso for their help with rhyolite-MELTS, and Alexander Nichols for his insightful comments during the development of this study. GS and BK were funded by the Royal Society Te Apārangi Marsden project “Shaking magma to trigger eruptions”. BVA acknowledges partial field support through ANID Millennium Science Initiative/Millennium Nucleus Paleoclimate NCN17_079. We thank the editor Alessandro Aiuppa, and Francisco Delgado and an anonymous reviewer for their constructive comments.

Appendix A. Supplementary data

Supplementary data to this article can be found online at https://doi.org/10.1016/j.jvolgeores.2021.107406.

References

Acocella, V., 2014. Great challenges in volcanology: how does the volcano factory work? Front. Earth Sci. 2, 1–10. https://doi.org/10.3389/feart.2014.00004.. http://journal.frontiersin.org/article/10.3389/feart.2014.00004/abstract.

Alloway, B.V., Pearce, N.J., Villarosa, G., Outes, V., Moreno, P.I., 2015. Multiple melt bodies fed the AD 2011 eruption of Puyehue-Cordón Caulle, Chile. Sci. Rep. 5, 1–8. https://doi.org/10.1038/srep17589.

Ayele, A., Jacques, E., Kassim, M., Kidane, T., Omar, A., Tait, S., Nercessian, A., de Chabalier, J.B., King, G., 2007. The volcano-seismic crisis in Afar, Ethiopia, starting September 2005. Earth Planet. Sci. Lett. 255, 177–187. https://doi.org/10.1016/j.epsl.2006.12.014.

Bachmann, O., Bergantz, G.W., 2008. Rhyolites and their source mushes across tectonic settings. J. Petrol. 49, 2277–2285. https://doi.org/10.1093/petrology/egn068.

Bachmann, O., Huber, C., 2016. Silicic magma reservoirs in the Earth's crust. Am. Mineral. 101, 2377–2404. https://doi.org/10.2138/am-2016-5675.

Baker, D.R., Alletti, M., 2012. Fluid saturation and volatile partitioning between melts and hydrous fluids in crustal magmatic systems: the contribution of experimental measurements and solubility models. Earth-Sci. Rev. 114, 298–324. https://doi.org/10.1016/j.earscirev.2012.06.005.

Barrientos, S.E., 1994. Large thrust earthquakes and volcanic eruptions. Pure Appl. Geophys. 142, 225–237. https://doi.org/10.1007/BF00875972.

Bertrand, S., Daga, R., Bedert, R., Fontijn, K., 2014. Deposition of the 2011–2012 Cordón Caulle tephra (Chile, 40°S) in lake sediments: implications for tephrochronology and volcanology. J. Geophys. Res.: Earth Surf. 119, 2555–2573. https://doi.org/10.1002/2014JF003321.

Biggs, J., Annen, C., 2019. The lateral growth and coalesence of magma systems. Philos. Trans. R. Soc. A: Math. Phys. Eng. Sci. 377. https://doi.org/10.1098/rsta.2018.0005.

Bonadonna, C., Cioni, R., Pistolesi, M., Elissondo, M., Baumann, V., 2015a. Sedimentation of long-lasting wind-affected volcanic plumes: the example of the 2011 rhyolitic Cordón Caulle eruption, Chile. Bull. Volcanol. 77, 13. https://doi.org/10.1007/s00445-015-0900-8.

Bonadonna, C., Pistolesi, M., Cioni, R., Degruyter, W., Elissondo, M., Baumann, V., 2015b. Dynamics of wind-affected volcanic plumes: the example of the 2011 Cordón Caulle eruption, Chile. J. Geophys. Res.: Solid Earth 120, 2242–2261. https://doi.org/10.1002/2014JB011478.

Bonali, F., Tibaldi, A., Corazzato, C., Tormey, D., Lara, L., 2013. Quantifying the effect of large earthquakes in promoting eruptions due to stress changes on magma pathway: the Chile case. Tectonophysics 583, 54–67. https://doi.org/10.1016/j.tecto.2012.10.025.. https://linkinghub.elsevier.com/retrieve/pii/S0040195112006890.

Bowen, N.L., 1915. The later stages of the evolution of the igneous rocks. J. Geol. 23, 1–91. https://doi.org/10.1086/622298.

Caricchi, L., Townsend, M., Rivalta, E., Namiki, A., 2021. The build-up and triggers of volcanic eruptions. Nat. Rev. Earth Environ. https://doi.org/10.1038/s43017-021-00174-8 0123456789. http://www.nature.com/articles/s43017-021-00174-8.

Cashman, K.V., Sparks, R.S.J., Blundy, J.D., 2017. Vertically extensive and unstable magmatic systems: a unified view of igneous processes. Science 355. https://doi.org/10.1126/science.aag3055.. http://science.sciencemag.org/content/355/6331/eaag3055.abstract.

Castro, J.M., Cordonnier, B., Schipper, C.I., Tuffen, H., Baumann, T.S., Feisel, Y., 2016. Rapid laccolith intrusion driven by explosive volcanic eruption. Nat. Commun. 7, 1–7. https://doi.org/10.1038/ncomms13585.

Castro, J.M., Dingwell, D.B., 2009. Rapid ascent of rhyolitic magma at Chaitén volcano, Chile. Nature 461, 780–783. https://doi.org/10.1038/nature08458.

Castro, J.M., Schipper, C.I., Mueller, S.P., Militzer, A.S., Amigo, A., Parejas, C.S., Jacob, D., 2013. Storage and eruption of near-liquidus rhyolite magma at Cordón Caulle, Chile. Bull. Volcanol. 75, 702. https://doi.org/10.1007/s00445-013-0702-9.

Cembrano, J., Hervé, F., Lavenu, A., 1996. The Liquiñe Ofqui fault zone: a long-lived intra-arc fault system in southern Chile. Tectonophysics 259, 55–66. https://doi.org/10.1016/0040-1951(95)00066-6.. https://linkinghub.elsevier.com/retrieve/pii/0040195195000666.

Cembrano, J., Lara, L.E., 2009. The link between volcanism and tectonics in the southern volcanic zone of the Chilean Andes: a review. Tectonophysics 471, 96–113. https://doi.org/10.1016/j.tecto.2009.02.038.

Chesley, C., La Femina, P.C., Puskas, C., Kobayashi, D., 2012. The 1707 M_w 8.7 Hoei earthquake triggered the largest historical eruption of Mt. Fuji. Geophys. Res. Lett. 39. https://doi.org/10.1029/2012GL053868 2012GL053868.

Cifuentes, I.L., 1989. The 1960 Chilean earthquakes. J. Geophys. Res. 94, 665–680. https://doi.org/10.1029/JB094iB01p00665.

Cooper, K.M., 2019. Time scales and temperatures of crystal storage in magma reservoirs: implications for magma reservoir dynamics. Philos. Trans. R. Soc. A: Math. Phys. Eng. Sci. 377. https://doi.org/10.1098/rsta.2018.0009.

Coppola, D., Laiolo, M., Franchi, A., Massimetti, F., Cigolini, C., Lara, L.E., 2017. Measuring effusion rates of obsidian lava flows by means of satellite thermal data. J. Volcanol. Geotherm. Res. 347, 82–90. https://doi.org/10.1016/j.jvolgeores.2017.09.003.

Daga, R., Ribeiro Guevara, S., Poire, D.G., Arribére, M., 2014. Characterization of tephras dispersed by the recent eruptions of volcanoes Calbuco (1961), Chaitén (2008) and Cordón Caulle Complex (1960 and 2011), in Northern Patagonia. J. S. Am. Earth Sci. 49, 1–14. https://doi.org/10.1016/j.jsames.2013.10.006.

Davis, M., Koenders, M.A., Petford, N., 2007. Vibro-agitation of chambered magma. J. Volcanol. Geotherm. Res. 167, 24–36. https://doi.org/10.1016/j.jvolgeores.2007.07.012.

Delgado, F., 2021. Rhyolitic volcano dynamics in the Southern Andes: contributions from 17 years of InSAR observations at Cordón Caulle volcano from 2003 to 2020. J. S. Am. Earth Sci. 106, 102841. https://doi.org/10.1016/j.jsames.2020.102841.. https://linkinghub.elsevier.com/retrieve/pii/S0895981120303849.

Delgado, F., Kubanek, J., Anderson, K., Lundgren, P., Pritchard, M., 2019. Physicochemical models of effusive rhyolitic eruptions constrained with InSAR and DEM data: a case study of the 2011–2012 Cordón Caulle eruption. Earth Planet. Sci. Lett. 524, 115736. https://doi.org/10.1016/j.epsl.2019.115736.

Delgado, F., Pritchard, M., Samsonov, S., Córdova, L., 2018. Renewed posteruptive uplift following the 2011–2012 rhyolitic eruption of Cordón Caulle (Southern Andes, Chile): evidence for transient episodes of magma reservoir recharge during 2012–2018. J. Geophys. Res.: Solid Earth 123, 9407–9429. https://doi.org/10.1029/2018JB016240.

Delgado, F., Pritchard, M.E., Basualto, D., Lazo, J., Córdova, L., Lara, L.E., 2016. Rapid reinflation following the 2011–2012 rhyodacite eruption at Cordón Caulle volcano (Southern Andes) imaged by InSAR: evidence for magma reservoir refill. Geophys. Res. Lett. 43, 9552–9562. https://doi.org/10.1002/2016GL070066.

Edmonds, M., Cashman, K.V., Holness, M., Jackson, M., 2019. Architecture and dynamics of magma reservoirs. Philos. Trans. R. Soc. A: Math. Phys. Eng. Sci. 377. https://doi.org/10.1098/rsta.2018.0298.

Foley, M.L., Miller, C.F., Gualda, G.A., 2020. Architecture of a super-sized magma chamber and remobilization of its basal cumulate (Peach Spring Tuff, USA). J. Petrol. 61. https://doi.org/10.1093/petrology/egaa020.

Gerlach, D.C., Frey, F.A., Moreno-Roa, H., Lopez-Escobar, L., 1988. Recent volcanism in the puyehue-cordon caulle region, Southern Andes, Chile (40.5°S): petrogenesis of evolved lavas. J. Petrol. 29, 333–382.

Ghiorso, M.S., Gualda, G.A.R., 2015. An H_2O-CO_2 mixed fluid saturation model compatible with rhyolite-MELTS. Contrib. Mineral. Petrol. 169, 53. https://doi.org/10.1007/s00410-015-1141-8.

Gualda, G.A., Ghiorso, M.S., 2014. Phase-equilibrium geobarometers for silicic rocks based on rhyolite-MELTS. Part 1: principles, procedures, and evaluation of the method. Contrib. Mineral. Petrol. 168, 1–17. https://doi.org/10.1007/s00410-014-1033-3.

Gualda, G.A., Ghiorso, M.S., Lemons, R.V., Carley, T.L., 2012. Rhyolite-MELTS: a modified calibration of MELTS optimized for silica-rich, fluid-bearing magmatic systems. J. Petrol. 53, 875–890. https://doi.org/10.1093/petrology/egr080.

Gualda, G.A., Gravley, D.M., Deering, C.D., Ghiorso, M.S., 2019. Magma extraction pressures and the architecture of volcanic plumbing systems. Earth Planet. Sci. Lett. 522, 118–124. https://doi.org/10.1016/j.epsl.2019.06.020.

Gualda, G.A.R., Ghiorso, M.S., 2015. MELTS_Excel: a microsoft excel-based MELTS interface for research and teaching of magma properties and evolution. Geochem. Geophys. Geosyst. 16, 315–324. https://doi.org/10.1002/2014GC005545.

Hantke, G., 1940. Das Vulkangebiet zwischen den Seen Ranco und Puyéhue in Süd-Chile. Bull. Volcanol. 7, 75–83. https://doi.org/10.1007/BF02994894.

Harmon, L.J., Cowlyn, J., Gualda, G.A., Ghiorso, M.S., 2018. Phase-equilibrium geobarometers for silicic rocks based on rhyolite-MELTS. Part 4: Plagioclase, orthopyroxene, clinopyroxene, glass geobarometer, and application to Mt. Ruapehu, New Zealand. Contrib. Mineral. Petrol. 173, 1–20. https://doi.org/10.1007/s00410-017-1428-z.

Holtzman, B., Groebner, N., Zimmerman, M.E., Ginsberg, S., Kohlstedt, D.L., 2003. Stress-driven melt segregation in partially molten rocks. Geochem. Geophys. Geosyst. 4, 8607. https://doi.org/10.1093/petrology/egp062.

Iacovino, K., Matthews, S., Wieser, P.E., Moore, G.M., Bégué, F., 2021. VESIcal Part I: an open-source thermodynamic model engine for mixed volatile (H2O-CO2) solubility in silicate melts. Earth Space Sci. https://doi.org/10.1029/2020EA001584.

Jarosewich, E., Nelen, J.A., Norberg, J.A., 1980. Reference samples for electron microprobe analysis. Geostand. Geoanal. Res. 4, 43–47. https://doi.org/10.1111/j.1751-908X.1980.tb00273.x.

Jay, J., Costa, F., Pritchard, M., Lara, L.E., Singer, B., Herrin, J., 2014. Locating magma reservoirs using InSAR and petrology before and during the 2011–2012 Cordón Caulle silicic eruption. Earth Planet. Sci. Lett. 395, 254–266. https://doi.org/10.1016/j.epsl.2014.03.046.

Katsui, Y., Katz, H.R., 1967. Lateral fissure eruptions in the Southern Andes of Chile. J. Fac. Sci. Hokkaido Univ. 13, 433–448.

Kavanagh, J.L., 2018. Mechanisms of Magma Transport in the Upper Crust-Dyking. Volcanic and Igneous Plumbing Systems. Elsevier, pp. 55–88 https://doi.org/10.1016/B978-0-12-809749-6.00003-0.. https://linkinghub.elsevier.com/retrieve/pii/B9780128097496000030.

Kennedy, B.M., Holohan, E.P., Stix, J., Gravley, D.M., Davidson, J.R., Cole, J.W., 2018. Magma plumbing beneath collapse caldera volcanic systems. Earth-Sci. Rev. 177, 404–424. https://doi.org/10.1016/j.earscirev.2017.12.002.

La Femina, P.C., Connor, C.B., Hill, B.E., Strauch, W., Saballos, J., 2004. Magma-tectonic interactions in Nicaragua: the 1999 seismic swarm and eruption of Cerro Negro volcano. J. Volcanol. Geotherm. Res. 137, 187–199. https://doi.org/10.1016/j.jvolgeores.2004.05.006.. https://linkinghub.elsevier.com/retrieve/pii/S0377027304001556.

Lara, L., Naranjo, J., Moreno, H., 2004. Rhyodacitic fissure eruption in Southern Andes (Cordón Caulle; 40.5°S) after the 1960 (Mw:9.5) Chilean earthquake: a structural interpretation. J. Volcanol. Geotherm. Res. 138, 127–138. https://doi.org/10.1016/j.jvolgeores.2004.06.009.. https://linkinghub.elsevier.com/retrieve/pii/S0377027304002136.

Lara, L.E., 2009. The 2008 eruption of the Chaitén Volcano, Chile: a preliminary report. Andean Geol. 36, 125–129. https://doi.org/10.4067/S0718-71062009000100009.. http://www.scielo.cl/scielo.php?script=sci_arttext&pid=S0718-71062009000100009&lng=en&nrm=iso&tlng=en.

Lara, L.E., Lavenu, A., Cembrano, J., Rodríguez, C., 2006a. Structural controls of volcanism in transversal chains: resheared faults and neotectonics in the Cordón Caulle-Puyehue area (40.5°S), Southern Andes. J. Volcanol. Geotherm. Res. 158, 70–86. https://doi.org/10.1016/j.jvolgeores.2006.04.017.

Lara, L.E., Moreno, H., Naranjo, J.A., Matthews, S., Pérez De Arce, C., 2006b. Magmatic evolution of the Puyehue-Cordón Caulle volcanic complex (40°S), Southern Andean Volcanic Zone: from shield to unusual rhyolitic fissure volcanism. J. Volcanol. Geotherm. Res. 157, 343–366. https://doi.org/10.1016/j.jvolgeores.2006.04.010.

Maldonado, V., Contreras, M., Melnick, D., 2021. A comprehensive database of active and potentially-active continental faults in Chile at 1:25,000 scale. Sci. Data 8, 1–13. https://doi.org/10.1038/s41597-021-00802-4.

Manga, M., Brodsky, E., 2006. Seismic triggering of eruptions in the far field: volcanoes and geysers. Annu. Rev. Earth Planet. Sci. 34, 263–291. https://doi.org/10.1146/annurev.earth.34.031405.125125.

Mingo, M.A., 2019. Evaluation of Pre-eruptive Conditions for Cordon Caulle Rhyo-Dacitic Historic Eruptions. Florida International University MSc thesis.

Moreno, M.S., Bolte, J., Klotz, J., Melnick, D., 2009. Impact of megathrust geometry on inversion of coseismic slip from geodetic data: application to the 1960 Chile earthquake. Geophys. Res. Lett. 36, L16310. https://doi.org/10.1029/2009GL039276.

Naranjo, J.A., Singer, B.S., Jicha, B.R., Moreno, H., Lara, L.E., 2017. Holocene tephra succession of Puyehue-Cordón Caulle and Antillanca/Casablanca volcanic complexes, southern Andes (40–41°S). J. Volcanol. Geotherm. Res. 332, 109–128. https://doi.org/10.1016/j.jvolgeores.2016.11.017.

Ojeda, J., Ruiz, S., del Campo, F., Carvajal, M., 2020. The 21 May 1960 M_W 8.1 Concepción earthquake: a deep megathrust foreshock that started the 1960 central-South Chilean seismic sequence. Seismol. Res. Lett. 91, 1617–1627. https://doi.org/10.1785/0220190143.

Paisley, R., Berlo, K., Whattam, J., Schipper, C.I., Tuffen, H., 2019. Degassing-induced chemical heterogeneity at the 2011–2012 Cordón Caulle eruption. Volcanica 2, 211–237. https://doi.org/10.30909/vol.02.02.211237.. https://www.jvolcanica.org/ojs/index.php/volcanica/article/view/38.

Pamukçu, A.S., Wright, K.A., Gualda, G.A., Gravley, D., 2020. Magma residence and eruption at the Taupo Volcanic Center (Taupo Volcanic Zone, New Zealand): insights from rhyolite-MELTS geobarometry, diffusion chronometry, and crystal textures. Contrib. Mineral. Petrol. 175, 1–27. https://doi.org/10.1007/s00410-020-01684-2.

Pistolesi, M., Cioni, R., Bonadonna, C., Elissondo, M., Baumann, V., Bertagnini, A., Chiari, L., Gonzales, R., Rosi, M., Francalanci, L., 2015. Complex dynamics of small-moderate volcanic events: the example of the 2011 rhyolitic Cordón Caulle eruption, Chile. Bull. Volcanol. 77. https://doi.org/10.1007/s00445-014-0898-3.

Pitcher, B.W., Gualda, G.A.R., Hasegawa, T., 2020. Repetitive duality of rhyolite compositions, timescales, and storage and extraction conditions for pleistocene caldera-forming eruptions, Hokkaido, Japan. J. Petrol. https://doi.org/10.1093/petrology/egaa106.

Saunders, K., Blundy, J., Dohmen, R., Cashman, K., 2012. Linking petrology and seismology at an active volcano. Science 336, 1023–1027. https://doi.org/10.1126/science.1220066 arXiv:arXiv:1308.5367.

Schipper, C.I., Castro, J., Kennedy, B., Christenson, B., Aiuppa, A., Alloway, B., Forte, P., Seropian, G., Tuffen, H., 2019. Halogen (Cl, F) release during explosive, effusive, and intrusive phases of the 2011 rhyolitic eruption at Cordón Caulle volcano (Chile). Volcanica 2, 73–90. https://doi.org/10.30909/vol.02.01.7390.. https://www.jvolcanica.org/ojs/index.php/volcanica/article/view/26.

Schipper, C.I., Castro, J.M., Kennedy, B.M., Tuffen, H., Whattam, J., Wadsworth, F.B., Paisley, R., Fitzgerald, R.H., Rhodes, E., Schaefer, L.N., Ashwell, P.A., Forte, P., Seropian, G., Alloway, B.V., 2021. Silicic conduits as supersized tuffisites: clastogenic influences on shifting eruption styles at Cordón Caulle volcano (Chile). Bull. Volcanol. 83. https://doi.org/10.1007/s00445-020-01432-1.

Schipper, C.I., Castro, J.M., Tuffen, H., James, M.R., How, P., 2013. Shallow vent architecture during hybrid explosive-effusive activity at Cordón Caulle (Chile, 2011–2012): evidence from direct observations and pyroclast textures. J. Volcanol. Geotherm. Res. 262, 25–37. https://doi.org/10.1016/j.jvolgeores.2013.06.005.

Sepúlveda, F., Dorsch, K., Lahsen, A., Bender, S., Palacios, C., 2004. Chemical and isotopic composition of geothermal discharges from the Puyehue-Cordón Caulle area (40.5°S), Southern Chile. Geothermics 33, 655–673. https://doi.org/10.1016/j.geothermics.2003.10.005.

Seropian, G., Kennedy, B.M., Walter, T.R., Ichihara, M., Jolly, A.D., 2021. A review framework of how earthquakes trigger volcanic eruptions. Nat. Commun. 12, 1004. https://doi.org/10.1038/s41467-021-21166-8.. http://www.nature.com/articles/s41467-021-21166-8.

Singer, B.S., Jicha, B.R., Harper, M.A., Naranjo, J.A., Lara, L.E., Moreno-Roa, H., 2008. Eruptive history, geochronology, and magmatic evolution of the Puyehue-Cordón Caulle volcanic complex, Chile. Geol. Soc. Am. Bull. 120, 599–618. https://doi.org/10.1130/B26276.1.. https://pubs.geoscienceworld.org/gsabulletin/article/120/5-6/599-618/2277.

Sparks, R.S.J., Annen, C., Blundy, J.D., Cashman, K.V., Rust, A.C., Jackson, M.D., 2019. Formation and dynamics of magma reservoirs. Philos. Trans. A https://doi.org/10.1098/rsta.2018.0019.

Sumita, I., Manga, M., 2008. Suspension rheology under oscillatory shear and its geophysical implications. Earth Planet. Sci. Lett. 269, 467–476. https://doi.org/10.1016/j.epsl.2008.02.043.

Tramontano, S., Gualda, G.A., Ghiorso, M.S., 2017. Internal triggering of volcanic eruptions: tracking overpressure regimes for giant magma bodies. Earth Planet. Sci. Lett. 472, 142–151. https://doi.org/10.1016/j.epsl.2017.05.014.

Tuffen, H., James, M.R., Castro, J.M., Schipper, C.I., 2013. Exceptional mobility of an advancing rhyolitic obsidian flow at Cordón Caulle volcano in Chile. Nat. Commun. 4, 1–7. https://doi.org/10.1038/ncomms3709.

Walter, T.R., 2007. How a tectonic earthquake may wake up volcanoes: stress transfer during the 1996 earthquake-eruption sequence at the Karymsky Volcanic Group, Kamchatka. Earth Planet. Sci. Lett. 264, 347–359. https://doi.org/10.1016/j.epsl.2007.09.006.. https://linkinghub.elsevier.com/retrieve/pii/S0012821X07005626.

Walter, T.R., Amelung, F., 2006. Volcano-earthquake interaction at Mauna Loa volcano, Hawaii. J. Geophys. Res. 111, B05204. https://doi.org/10.1029/2005JB003861.

Walter, T.R., Amelung, F., 2007. Volcanic eruptions following M ≥ 9 megathrust earthquakes: implications for the Sumatra-Andaman volcanoes. Geology 35, 539–542. https://doi.org/10.1130/G23429A.1.

Watt, S.F.L., Pyle, D.M., Mather, T.A., 2009. The influence of great earthquakes on volcanic eruption rate along the Chilean subduction zone. Earth Planet. Sci. Lett. 277, 399–407. https://doi.org/10.1016/j.epsl.2008.11.005.

Wendt, A., Tassara, A., Báez, J.C., Basualto, D., Lara, L.E., García, F., 2017. Possible structural control on the 2011 eruption of Puyehue-Cordón Caulle Volcanic Complex (southern Chile) determined by InSAR, GPS and seismicity. Geophys. J. Int. 208, 134–147. https://doi.org/10.1093/gji/ggw355.. https://academic.oup.com/gji/article/208/1/134/2452666.

Zhang, C., Koepke, J., Wang, L.X., Wolff, P.E., Wilke, S., Stechern, A., Almeev, R., Holtz, F., 2016. A practical method for accurate measurement of trace level fluorine in Mg- and Fe-bearing minerals and glasses using electron probe microanalysis. Geostand. Geoanal. Res. 40, 351–363. https://doi.org/10.1111/j.1751-908X.2015.00390.x.